

Contents

I. Types of Rydberg Interactions	1
II. Analytical Results	2
III. Symmetry protection of the phase	4
IV. Approximate analytical solution including absorption	5
V. Modeling the complete experiment	9
VI. Obtaining observables from numerical simulations	13
VII. Spin wave dephasing due to Rydberg-ground state atom interactions	15
VIII. Methods	17
References	19

I. TYPES OF RYDBERG INTERACTIONS

The interaction between two atoms in distinct levels Rydberg levels R and R' has the general form

$$V = \begin{pmatrix} V_b(r) & V_{ex}(r) \\ V_{ex}(r) & V_b(r) \end{pmatrix} \quad (1)$$

in the two-atom product basis $\{|RR'\rangle, |R'R\rangle\}$. Here, r is the distance between the atoms.

For levels R, R' with $\Delta L = \pm 1$, the dominant interaction will be the direct dipolar interaction $V_{ex}(r) = C_3/r^3$ [1]. Because this interaction is not diagonal in the product basis, its action is to exchange the states $|RR'\rangle$ and $|R'R\rangle$. This case describes the interaction between the $|100S_{1/2}, m_J = 1/2\rangle$ and $|99P_{3/2}, m_J = 3/2\rangle$ states used for the experiments in the main text, which feature $C_3/h = 33.4 \text{ GHz } \mu\text{m}^3$. For these states, V_b is negligible at the relevant length scales (less than 5% of V_{ex} at $r = 20 \mu\text{m}$), as shown in Fig. S1.

In contrast, for same-parity levels, the direct dipolar interaction is not allowed, so the dominant interaction is second-order, such that $V_b(r) = C_6/r^6$ and $V_{ex}(r) = \chi_6/r^6$. For states with widely separated principal quantum numbers, $|C_6| \gg |\chi_6|$. However, if the principal quantum numbers of the R, R' states are similar, $|\chi_6|$ can be comparable to $|C_6|$. When $|C_6| \gg |\chi_6|$, the interaction does not lead to exchange of Rydberg excitations, but only shifts the combined

*These authors contributed equally to this work

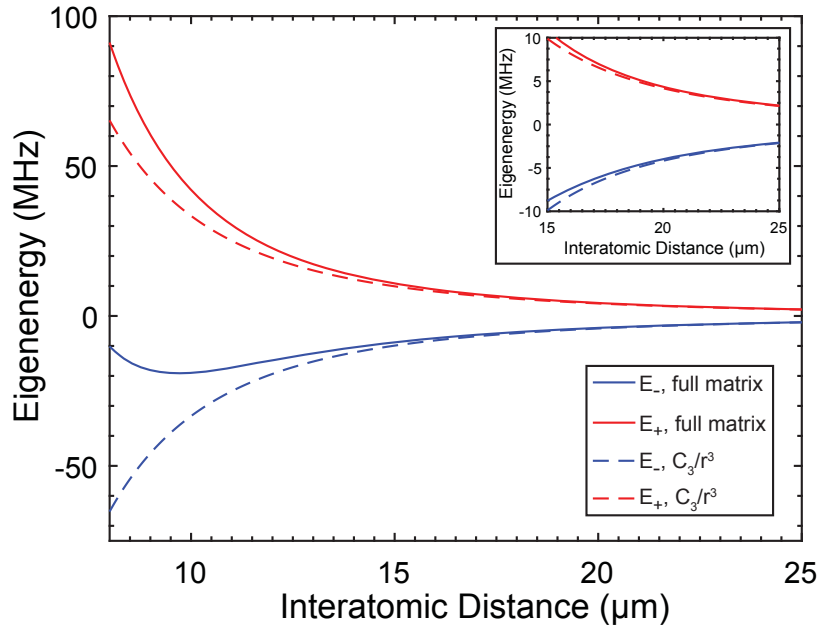


FIG. S1: Comparison of eigenenergies of a $|100S_{1/2}, m_J = 1/2\rangle - |99P_{3/2}, m_J = 3/2\rangle$ atom pair using numerical diagonalization of the dipolar Hamiltonian in a basis of 2750 pairs of Rydberg levels, and a C_3/r^3 approximation (dashed lines). The positive and negative eigenenergies, E_+ and E_- (corresponding to the *gerade* and *ungerade* molecular states), are plotted as a function of the distance between the atoms r , relative to their average energy when $r \rightarrow \infty$. The C_3 approximation is accurate to better than 5% at distances greater than 20 μm , which is where the exchange interaction takes place at the highest densities used in the experiment.

energy, as is typically assumed for Rydberg blockade (and must be true when $R = R'$). In contrast, when $|\chi_6| \approx |C_6|$ state exchange is also possible.

For the experiments described in the inset to Fig. 3, the state $|97S_{1/2}\rangle$ has $C_6/h = -114 \text{ THz } \mu\text{m}^6$ and $\chi_6/h = -0.6 \text{ THz } \mu\text{m}^6$, while $|99S_{1/2}\rangle$ has $C_6/h = 65.3 \text{ THz } \mu\text{m}^6$ and $\chi_6/h = 48.7 \text{ THz } \mu\text{m}^6$. These values are obtained from direct diagonalization of the dipole-dipole Hamiltonian for a truncated basis of states [1]. All potentials are evaluated for interatomic separation along the quantization axis, which is appropriate for the quasi-1D geometry of the experiment.

II. ANALYTICAL RESULTS

In this section, we provide the theory of photon exchange process. We will focus on the derivation of the effective Schrödinger equation provided in the main text and its analytical solution. We shall see that such model is asymptotically valid in the limit of large atomic density. A more rigorous theoretical treatment of the problem, including the effects of inhomogeneous density of the atomic cloud and the finite lifetime of Rydberg states, is provided in section IV.

The dynamics in our system are described by a Hamiltonian $\hat{H} = \hat{H}_{\text{EIT}} + \hat{V}_{\text{ex}}$, where \hat{H}_{EIT} and \hat{V}_{ex} characterize the propagation and the interaction of photons, respectively. In the rotating frame, this Hamiltonian can be efficiently written in terms of bosonic field operators $\hat{\mathcal{E}}^\dagger(z)$, $\hat{\mathcal{P}}^\dagger(z)$, $\hat{\mathcal{S}}^\dagger(z)$, and $\hat{\mathcal{C}}^\dagger(z)$ for a signal photon, an atomic excitation in the $5P_{3/2}$ state, an excitation in the nS state, and an excitation in the $n'P$ state (the gate photon) [2]:

$$\hat{H}_{\text{EIT}} = \int dz \left(\hat{\mathcal{E}}^\dagger(z), \hat{\mathcal{P}}^\dagger(z), \hat{\mathcal{S}}^\dagger(z) \right) \begin{pmatrix} -ic\partial_z & \bar{g} & 0 \\ \bar{g} & -i\gamma & \Omega \\ 0 & \Omega & 0 \end{pmatrix} \begin{pmatrix} \hat{\mathcal{E}}(z) \\ \hat{\mathcal{P}}(z) \\ \hat{\mathcal{S}}(z) \end{pmatrix} \quad (2)$$

and

$$\hat{V}_{\text{ex}} = \int dx dy V(x-y) \hat{\mathcal{C}}^\dagger(y) \hat{\mathcal{S}}^\dagger(x) \hat{\mathcal{S}}(y) \hat{\mathcal{C}}(x), \quad (3)$$

where c is the speed of light, \bar{g} is the collectively enhanced coupling of a signal photon to the ensemble of atoms, Ω is the Rabi frequency of the control field laser, γ is the decay rate of the $5P_{3/2}$ state, and $V(r) = C_\alpha/r^\alpha$ is the strength of the long-range interaction. \hat{V}_{ex} can arise from a dipolar ($\alpha = 3$) or van der Waals interaction ($\alpha = 6$), but we concentrate on the $\alpha = 3$ case here. We use units such that $\hbar = 1$. Note that the relationship to the experimental units in the main text is $\Omega = \Omega_c/2$ and $\gamma = \Gamma/2$, where $\Gamma/(2\pi) = 6.1$ MHz for Rb. The EIT linewidth used in the main text is defined as $\gamma_{\text{EIT}} = \Omega_c^2/\Gamma$.

Owing to EIT, photons propagate as dark state polaritons in the atomic cloud, so we introduce the dark and bright polariton basis $\hat{\mathcal{D}}(z) = \cos\theta\hat{\mathcal{S}}(z) - \sin\theta\hat{\mathcal{E}}(z)$ and $\hat{\mathcal{B}}(z) = \sin\theta\hat{\mathcal{S}}(z) + \cos\theta\hat{\mathcal{E}}(z)$. Here the mixing angle is given by $\sin\theta \equiv \Omega/\sqrt{\bar{g}^2 + \Omega^2}$ [3], and in our system, $\theta \ll 1$ by several orders of magnitude. The propagation of the dark state polariton is well described by a Hamiltonian

$$\hat{H}_D = -i \int dz v_g \hat{\mathcal{D}}^\dagger(z) \partial_z \hat{\mathcal{D}}(z) \quad (4)$$

with the slow light group velocity $v_g = c \Omega^2/(\bar{g}^2 + \Omega^2)$. The reduced group velocity arises from the fact that the polariton is composed of atomic and photonic components, and a larger atomic component will result in slower light [3]. Also, in this basis, the interaction becomes

$$\hat{V}_{\text{ex}} = \int dx dy \cos^2\theta V(x-y) \hat{\mathcal{C}}^\dagger(y) \hat{\mathcal{D}}^\dagger(x) \hat{\mathcal{D}}(y) \hat{\mathcal{C}}(x) + \mathcal{O}(\sin\theta), \quad (5)$$

where we may only keep the leading order term with an approximation $\cos\theta \approx 1$. These approximations are valid as long as bright state polaritons or $5P_{3/2}$ states are not populated, which we will confirm for self-consistency. In order to describe the photon collision dynamics, we define a two-photon wavefunction $\psi(r, r')$ as the probability amplitude of finding a dark state polariton (signal photon) at r and a $n'P$ excitation (gate photon) at r' , namely $\psi(r, r') = \langle 0 | \hat{\mathcal{D}}(r) \hat{\mathcal{C}}(r') | \psi \rangle$. Then, the time evolution of the wavefunction can be obtained from the Schrödinger equation

$$\frac{\partial}{\partial t} \psi(r, r') = \langle 0 | \hat{\mathcal{D}}(r) \hat{\mathcal{C}}(r') \frac{\partial}{\partial t} | \psi \rangle = -i \langle 0 | \hat{\mathcal{D}}(r) \hat{\mathcal{C}}(r') (\hat{H}_D + \hat{V}_{\text{ex}}) | \psi \rangle \quad (6)$$

$$= -v_g \frac{\partial}{\partial r} \psi(r, r') - iV(r-r') \psi(r, r'), \quad (7)$$

where we recover Eq. (1) from the main text. To obtain the second line, we have used the commutation relations of bosonic field operators, e.g.,

$$\langle 0 | \hat{\mathcal{D}}(r) \hat{\mathcal{C}}(r') \hat{H}_D | \psi \rangle = -i \int dz v_g \langle 0 | \hat{\mathcal{D}}(r) \hat{\mathcal{D}}^\dagger(z) \partial_z \hat{\mathcal{D}}(z) \hat{\mathcal{C}}(r') | \psi \rangle \quad (8)$$

$$= -i \int dz v_g \langle 0 | \left(\hat{\mathcal{D}}^\dagger(z) \hat{\mathcal{D}}(r) + \delta(z-r) \right) \partial_z \hat{\mathcal{D}}(z) \hat{\mathcal{C}}(r') | \psi \rangle \quad (9)$$

$$= -iv_g \partial_r \langle 0 | \hat{\mathcal{D}}(r) \hat{\mathcal{C}}(r') | \psi \rangle = -iv_g \partial_r \psi(r, r'), \quad (10)$$

and similarly for $\langle 0 | \hat{\mathcal{D}}(r) \hat{\mathcal{C}}(r') \hat{V}_{\text{ex}} | \psi \rangle$.

Now, we solve the Schrödinger equation in Eq. (7). Note that the exchange interaction is not in the conventional form since it couples two wavefunction amplitudes at reversed positions $r \leftrightarrow r'$. In order to convert this into a local interaction, we divide the wavefunction into two components $\psi(r, r') = \psi_{SP}(r, r')$ for $r < r'$ and $\psi(r, r') = \psi_{PS}(r', r)$ for $r > r'$, where our Schrödinger's equation becomes

$$i \frac{\partial}{\partial t} \begin{pmatrix} \psi_{SP} \\ \psi_{PS} \end{pmatrix} = \begin{pmatrix} -iv_g \partial_r & V_{\text{ex}}(r-r') \\ V_{\text{ex}}(r-r') & -iv_g \partial_{r'} \end{pmatrix} \begin{pmatrix} \psi_{SP} \\ \psi_{PS} \end{pmatrix}. \quad (11)$$

Then, we move into the center of mass frame by introducing $R = (r+r')/2$ and $z = r' - r$, where the propagation is described by $\partial_r \mapsto \frac{1}{2}\partial_R - \partial_z$ and $\partial_{r'} \mapsto \frac{1}{2}\partial_R + \partial_z$. Finally, introducing a new effective time variable $\partial_\tau \equiv \partial_t + \frac{v_g}{2}\partial_R$ in this frame, we obtain

$$i \frac{\partial}{\partial \tau} \begin{pmatrix} \psi_{SP} \\ \psi_{PS} \end{pmatrix} = \begin{pmatrix} iv_g \partial_z & V_{\text{ex}}(z) \\ V_{\text{ex}}(z) & -iv_g \partial_z \end{pmatrix} \begin{pmatrix} \psi_{SP} \\ \psi_{PS} \end{pmatrix} = [i\sigma^z v_g \partial_z + V(z)\sigma^x] \begin{pmatrix} \psi_{SP} \\ \psi_{PS} \end{pmatrix}, \quad (12)$$

where σ^μ are the Pauli operators.

In the continuous-wave limit (where the R dependence vanishes), we are interested in the properties of the zero-energy eigenstates of this equation, which describe the interaction between photons with vanishing relative momentum. By setting the left hand side of Eq. (12) to zero and multiplying by σ^z , we obtain $-iv_g\partial_z\Psi = iV_{ex}(z)\sigma^y\Psi$ with $\Psi = (\psi_{SP}, \psi_{PS})^T$. We integrate from $z = \infty$ to $z = z'$ to get

$$\Psi(z') = e^{-\frac{1}{v_g}\int_{\infty}^{z'} V_{ex}(z)dz\sigma^y} \Psi(\infty) = \begin{pmatrix} \cosh \phi(z') & -i \sinh \phi(z') \\ i \sinh \phi(z') & \cosh \phi(z') \end{pmatrix} \Psi(\infty), \quad (13)$$

with $\phi(z') \equiv \frac{1}{v_g} \int_{z'}^{\infty} V_{ex}(z)dz$. For a normalizable solution, we require that $|\Psi(z')| < \infty$ as $z' \rightarrow 0$. Since $\phi(z')$ diverges for decreasing z' , such a solution is possible only when $\Psi(\infty) \propto (1, -i)$ for positive C_α and $\Psi(\infty) \propto (1, i)$ for negative C_α . Therefore, the zero energy eigenstate is given by

$$\begin{pmatrix} \psi_{SP} \\ \psi_{PS} \end{pmatrix} \propto \begin{pmatrix} e^{-|\phi(z')|} \\ -\text{sign}(C_\alpha)ie^{-|\phi(z')|} \end{pmatrix}. \quad (14)$$

For a dipolar interaction, this solution reduces to

$$\psi(r, r') = e^{-\frac{1}{2v_g} \frac{|C_3|}{(r-r')^2}} e^{-i \text{sign}[(r-r')C_3]\pi/4}. \quad (15)$$

By defining the hopping length scale $r_s \equiv \sqrt{|C_3|/v_g}$, we recover the solution following Eq. (1) in the main text. This can also be expressed in terms of the blockade radius as $r_s = \sqrt{OD_b/2}r_b$, where $r_b = (|C_3|\gamma/\Omega^2)^{1/3}$ and $OD_b = r_b/l_a$, with l_a being the attenuation length for the probe field in the absence of EIT (inversely proportional to the atomic density).

There are several points worth noting. First, Eq. (15) implies that the particle propagates as a (zero momentum) plane wave at $r \rightarrow \pm\infty$. The relative phase difference between these two plane waves $\psi_{SP}(z = \infty)$ (before the collision) and $\psi_{PS}(z = \infty)$ (after the collision) indicates that the interaction imprints a phase of $\pm\pi/2$ for positive and negative C_α , respectively. Second, this wavefunction has vanishingly small amplitude when $|r - r'| < r_s$. Therefore, the bright state polaritons or $5P_{3/2}$ states will not be populated when $OD_b \gg 1$, consistent with our initial assumptions. Finally, we note that the imprinted phase $\pm\pi/2$ is independent of the precise value of experimental parameters such as Ω, \bar{g}, γ or $V_{ex}(r - r')$. The only requirement for the phase being unchanged is that the integrated interaction $\phi(z)$ diverges as z approach zero. While this is approximately satisfied in the regime of large OD_b , more careful analysis is necessary for small OD_b , as we provide later in section IV.

III. SYMMETRY PROTECTION OF THE PHASE

The fact that the phase shift acquired in a collision between two polaritons is robustly $\pi/2$, independent of the precise experimental parameters, can be understood in terms of symmetries of the effective Hamiltonian describing the scattering process. To derive this, we start with the effective Schrödinger equation from the previous section:

$$i\partial_\tau\Psi = [i\sigma^z v_g\partial_z + V(z)\sigma^x]\Psi \equiv \hat{H}_{ex}\Psi, \quad (16)$$

where z is the distance between two particles, Ψ is the two-component wavefunction $\Psi = (\psi_{SP}, \psi_{PS})^T$, and τ is the effective time in the center-of-mass frame defined by $\partial_\tau = \partial_t + (v_g/2)\partial_R$. We find that this effective Hamiltonian \hat{H}_{ex} has three symmetries $\hat{\mathbb{T}}, \hat{\mathbb{P}}$, and $\hat{\mathbb{C}}$, whose action on the wavefunction is defined by:

$$\hat{\mathbb{T}} = \sigma^x \hat{\mathbb{K}}, \quad \hat{\mathbb{P}} = \sigma^z \hat{\mathbb{K}}, \quad \hat{\mathbb{C}} = -i\sigma^y, \quad (17)$$

where $\hat{\mathbb{K}}$ is complex conjugation. We refer to these symmetries as time-reversal, particle-hole, and chiral symmetries (respective) in analogy to those of fermionic particles. Note that three operators are related by $\hat{\mathbb{C}} \equiv \hat{\mathbb{T}}\hat{\mathbb{P}}$ as in the case of free fermions. The symmetry of the exchange process is defined by the commutation and anti-commutation relations of \hat{H}_{ex} with these operators, where one can easily check that

$$\hat{\mathbb{T}}\hat{H}_{ex} = \hat{H}_{ex}\hat{\mathbb{T}}, \quad \hat{\mathbb{P}}\hat{H}_{ex} = -\hat{H}_{ex}\hat{\mathbb{P}}, \quad \hat{\mathbb{C}}\hat{H}_{ex} = -\hat{H}_{ex}\hat{\mathbb{C}}. \quad (18)$$

These symmetries imply that if Ψ is an eigenstate of H_{ex} with energy E , then $\hat{\mathbb{T}}\Psi, \hat{\mathbb{P}}\Psi, \hat{\mathbb{C}}\Psi$ are also eigenstates with energy $E, -E$, and $-E$, respectively. Here, we are most interested in a propagating wave at energy $E = 0$, where any linear combination of these states are still an eigenstate with zero energy. Let us assume $\Psi_0 = (f(z), g(z))^T$ is such an

eigenstate. As the interaction $V(z)$ diverges at $z = 0$ and vanishes at $z \rightarrow \infty$, we know $f(z)$ and $g(z)$ have to vanish at $z = 0$ and converge at large z to a plane wave with zero momentum (i.e., a constant). Without loss of generality, we set $f(\infty) = 1$ and $g(\infty) = t$, where t is the complex transmission coefficient. From the time-reversal symmetry, it follows that the wavefunction $\Psi_1 \equiv t^* \Psi_0 - \hat{\mathbb{T}} \Psi_0 = [t^* f(z) - g^*(z), t^* g(z) - f^*(z)]^T$ is an eigenstate, where the first component vanishes as $z \rightarrow \infty$. Using the conservation of the probability current densities at $z = 0$ and $z = \infty$, one finds that the second component must also vanish, implying that the transmission probability is unity $|t|^2 = 1$. It follows that, to the extent that the above symmetries are perfectly satisfied, the transmission through the medium in the presence of the exchange interaction is perfectly lossless.

Similarly, using the particle-hole and chiral symmetries, one can define $\Psi_2 \equiv \Psi_0 + \hat{\mathbb{P}} \Psi_0$ and $\Psi_3 \equiv t \Psi_0 - \hat{\mathbb{C}} \Psi_0$, each of which implies $t + t^* = 0$ and $t^2 + 1 = 0$, respectively. Thus the combination of the particle-hole and chiral symmetries ensures that the scattering phase of the collision is $\pm\pi/2$. Table I summarizes the symmetry properties

Symmetry	Properties	Action (single-component)	Action (two-component)	Consequence
Time-reversal	anti-unitary $\hat{\mathbb{T}} \hat{H} = \hat{H} \hat{\mathbb{T}}$	$\psi(r, r') \mapsto \psi^*(r', r)$	$\sigma^x \hat{\mathbb{K}}$	$ t ^2 = 1$
Particle-hole	anti-unitary $\hat{\mathbb{P}} \hat{H} = -\hat{H} \hat{\mathbb{P}}$	$\psi(r, r') \mapsto \text{sgn}(r' - r) \psi^*(r, r')$	$\sigma^z \hat{\mathbb{K}}$	$t + t^* = 0$
Chiral	unitary $\hat{\mathbb{C}} \hat{H} = -\hat{H} \hat{\mathbb{C}}$	$\psi(r, r') \mapsto -\text{sgn}(r' - r) \psi(r', r)$	$-i\sigma^y$	$t^2 = -1$

TABLE I: Summary of symmetries and their consequences. The operator $\hat{\mathbb{K}}$ indicates complex-conjugation.

of our collision process and their consequences.

Interestingly, if $V_{ex}(z)$ does not diverge at $z = 0$, this symmetry argument is broken due to the boundary condition $\lim_{z \rightarrow 0} f(z) = \lim_{z \rightarrow 0} g(z)$. If $f(0) = g(0) \neq 0$ satisfies the boundary condition, $\hat{\mathbb{C}} \Psi$ or $\hat{\mathbb{P}} \Psi$ cannot, breaking the symmetries. When $V(0)$ diverges, the value of $|\Psi(0)|$ vanishes and the symmetry is restored, providing a robust phase shift.

IV. APPROXIMATE ANALYTICAL SOLUTION INCLUDING ABSORPTION

Here, we consider a complete model for polariton collisions that allows for the incorporation of loss and finite pulse bandwidth effects. We first use this model to derive approximate analytical expressions for the loss and phase shift for continuous-wave fields in the limits of small and large OD_b , and then consider the impact of finite pulse bandwidth.

From Eqs. (2) and (3) we can derive the following Heisenberg equations for the slowly-varying bosonic operators $\{\hat{\mathcal{E}}, \hat{\mathcal{P}}, \hat{\mathcal{S}}, \hat{\mathcal{C}}\}$:

$$(\partial_t + c\partial_z) \hat{\mathcal{E}}(z, t) = -i\bar{g} \hat{\mathcal{P}}(z, t) \quad (19)$$

$$\partial_t \hat{\mathcal{P}}(z, t) = -i\bar{g} \hat{\mathcal{E}}(z, t) - i\Omega \hat{\mathcal{S}}(z, t) - \gamma \hat{\mathcal{P}}(z, t) \quad (20)$$

$$\partial_t \hat{\mathcal{S}}(z, t) = -i\Omega \hat{\mathcal{P}}(z, t) - i \int dz' V(z - z') \hat{\mathcal{C}}^\dagger(z', t) \hat{\mathcal{C}}(z, t) \hat{\mathcal{S}}(z', t) \quad (21)$$

$$\partial_t \hat{\mathcal{C}}(z, t) = -i \int dz' V(z - z') \hat{\mathcal{S}}(z', t) \hat{\mathcal{S}}^\dagger(z, t) \hat{\mathcal{C}}(z', t) \quad (22)$$

The interaction between a single signal and gate photon can be described by the two-body wavefunction:

$$|\psi_2(t)\rangle = \int dz dz' EC(z, z', t) \hat{\mathcal{E}}^\dagger(z) \hat{\mathcal{C}}^\dagger(z') |0\rangle + \int dz dz' PC(z, z', t) \hat{\mathcal{P}}^\dagger(z) \hat{\mathcal{C}}^\dagger(z') |0\rangle \\ + \int dz dz' SC(z, z', t) \hat{\mathcal{S}}^\dagger(z) \hat{\mathcal{C}}^\dagger(z') |0\rangle. \quad (23)$$

Here the amplitudes $EC(z, z', t) = \langle 0 | \hat{\mathcal{E}}(z) \hat{\mathcal{C}}(z') | \psi(t) \rangle$, $PC(z, z', t) = \langle 0 | \hat{\mathcal{P}}(z) \hat{\mathcal{C}}(z') | \psi(t) \rangle$, and $SC(z, z', t) = \langle 0 | \hat{\mathcal{S}}(z) \hat{\mathcal{C}}(z') | \psi(t) \rangle$ correspond, respectively, to a signal photon, intermediate state, or nS -Rydberg excitation at

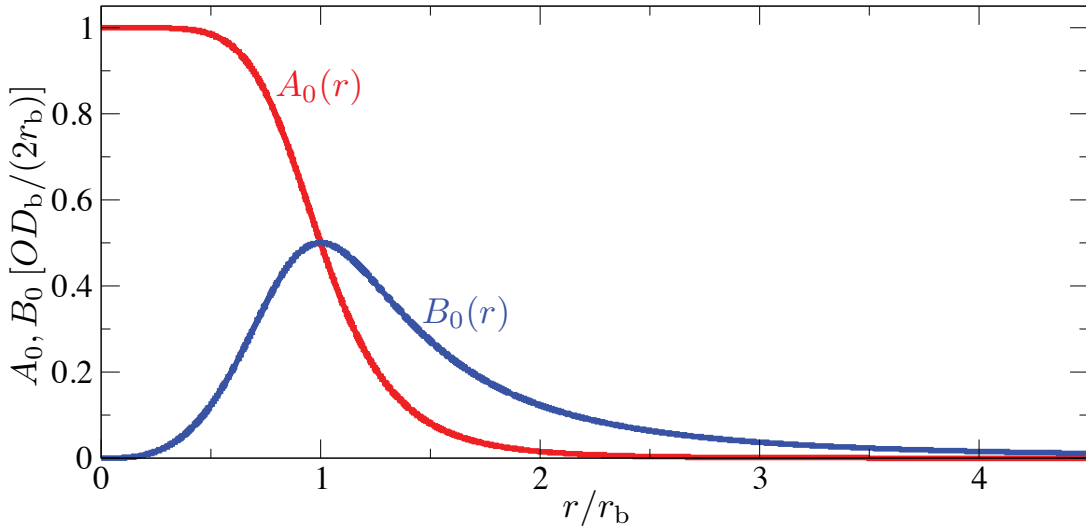


FIG. S2: Loss coefficient (red) and hopping strength (blue) as given by Eqs. (28) in the limit of a very slowly propagating polariton, $\omega = K = 0$.

position z , with the $n'P$ spin wave stored at position z' . Their evolution equations follow by substitution into Eqs. (19)-(22), which gives

$$\begin{aligned} (\partial_t + c\partial_z)EC(z, z', t) &= -i\bar{g}PC(z, z', t) \\ \partial_t PC(z, z', t) &= -i\bar{g}EC(z, z', t) - i\Omega SC(z, z', t) - \gamma PC(z, z', t) \\ \partial_t SC(z, z', t) &= -i\Omega PC(z, z', t) - i\frac{C_3}{|z - z'|^3} SC(z, z', t). \end{aligned} \quad (24)$$

Transforming into the center-of-mass frame with $r = |z - z'|$ and $R = z + z'$ and Fourier transforming the resulting equations with respect to time and R ($t \rightarrow \omega$ and $R \rightarrow K$) one can derive a single equation for $\psi \equiv EC$

$$\partial_r \psi(\pm r, K, \omega) = \pm A(r, \omega) \psi(\pm r, K, \omega) \pm iB(r, \omega) \psi(\mp r, K, \omega) \quad (25)$$

with the complex coefficients

$$\begin{aligned} A(r, K, \omega) &= i\frac{\bar{g}^2}{c(\omega - i\gamma)} - iK - i\frac{\omega}{c} + i\frac{\bar{g}^2\Omega^2}{c(\omega - i\gamma)^2} \frac{\omega - \frac{\Omega^2}{\omega - i\gamma}}{\left(\omega - \frac{\Omega^2}{\omega - i\gamma}\right)^2 - V(r)^2} \\ B(r, \omega) &= \frac{\bar{g}^2\Omega^2}{c(\omega - i\gamma)^2} \frac{V(r)}{\left(\omega - \frac{\Omega^2}{\omega - i\gamma}\right)^2 - V(r)^2}. \end{aligned} \quad (26)$$

Since $r \geq 0$, the wave function is defined such that $\psi(-r)$ and $\psi(+r)$ describe a signal photon propagating towards and away from the spin wave, respectively.

The advantage of such a splitting of the position-space is that the two sectors are related by the complex transmission amplitude $T(r, K, \omega) = \psi(+r)/\psi(-r)$, for which one obtains a closed equation

$$\partial_r T = 2AT + iB(1 + T^2), \quad (27)$$

subject to the initial condition $T(r = 0, K, \omega) = 1$. While Eq. (27) does not feature a general analytical solution, one can treat several important limiting cases as described below.

A. Absorptionless solution in the cw-limit

For long (quasi-continuous) signal and gate pulses we may take Eqs. (26) at $\omega = K = 0$ such that the coefficients become real

$$A_0(r) = A(r, 0, 0) = -\frac{OD_b}{2r_b} \frac{r_b^6}{r_b^6 + r^6}, \quad B_0(r) = B(r, 0, 0) = \frac{OD_b}{2r_b} \frac{r_b^3 r^3}{r_b^6 + r^6}. \quad (28)$$

This equation shows that $B_0(r)$ corresponds to the strength of the coherent hopping while the coefficient $A_0(r)$ causes photon loss, i.e. linearly damps the transmission amplitude in Eq.(27). Since $A_0 \sim r^{-6}$ drops much more rapidly than $B_0 \sim r^{-3}$ for large distances $r \gg r_b$ (see Fig. S2), we may neglect the A_0 to obtain a particularly simple solution

$$T_0(r) = \tan \left[\frac{\pi}{4} + i \int_0^r B_0(r') dr' \right], \quad (29)$$

of Eq.(27). Indeed there is no absorption in this limit since $T_0(r) = e^{i\varphi(r)}$. The accumulated phase of the outgoing photon

$$\varphi_0(\infty) = \text{acos} \left[\cosh \left(OD_b \frac{\sqrt{3}}{9} \pi \right)^{-1} \right] \xrightarrow{OD_b \gg 1} \frac{\pi}{2} - 2e^{-OD_b \frac{\sqrt{3}}{9} \pi}, \quad (30)$$

exponentially approaches $\pi/2$ for a large optical depth per blockade radius OD_b . Substituting the calculated transmission amplitude into Eq. (25) and using Eq. (27) we can also determine the actual wave function

$$\psi(\pm r) = \frac{\cosh \left[\int_0^r B_0(r') dr' \right] \pm i \sinh \left[\int_0^r B_0(r') dr' \right]}{\cosh \left[OD_b \frac{\sqrt{3}}{18} \pi \right] - i \sinh \left[OD_b \frac{\sqrt{3}}{18} \pi \right]} \psi(-\infty). \quad (31)$$

For large distances $r \gg r_b$ we can approximate $B_0(r) \approx \frac{OD_b}{2} \frac{r_b^2}{r^3}$ to solve the involved integral

$$\int_0^r B_0(r') dr' \approx \int_0^\infty B_0(r') dr' - \frac{OD_b}{2} r_b^2 \int_r^\infty r'^{-3} dr' = OD_b \left(\frac{\sqrt{3}\pi}{18} - \frac{r_b^2}{4r^2} \right) \quad (32)$$

and obtain the asymptotic solution

$$\begin{aligned} \psi(\pm r) &\underset{r \gg r_b}{\approx} \frac{\cosh \left[OD_b \left(\frac{\sqrt{3}\pi}{18} - \frac{r_b^2}{4r^2} \right) \right] \pm i \sinh \left[OD_b \left(\frac{\sqrt{3}\pi}{18} - \frac{r_b^2}{4r^2} \right) \right]}{\cosh \left[OD_b \frac{\sqrt{3}}{18} \pi \right] - i \sinh \left[OD_b \frac{\sqrt{3}}{18} \pi \right]} \psi(-\infty) \\ &\underset{OD_b \gg 1}{\approx} \frac{1 \pm i}{1 - i} e^{-OD_b \frac{r_b^2}{4r^2}} \psi(-\infty) \end{aligned} \quad (33)$$

which for $OD \gg 1$ approaches the solution given in the main text. As shown in Fig. S3, this solution provides a reasonably good description of the numerical results already for moderate values of OD_b , while the vanishing of $\psi(r)$ for $r < r_b$ provides a self-consistency test of the applied approximations. The main difference between the analytical solution and the numerical result stems from the photon losses for which we will now derive an analytical estimate.

B. Leading-order absorption

The simple solution permits us to determine the residual photon loss in the limit of large OD_b by perturbatively accounting for the amplitude decay coefficient $A_0(r)$. Using standard perturbation theory with $A_0(r)$ as the small parameter, the leading correction to the transmission amplitude is obtained from

$$\partial_r T_1(r) = 2A_0(r)T_0(r) + iB_0(r)2T_0(r)T_1(r), \quad (34)$$

which subject to the boundary condition $T_1(0) = 0$ has the following solution

$$T_1(r) = 2 \frac{\int_0^r A_0(z') \cosh \left[2 \int_0^{z'} B_0(z'') dz'' \right] dz'}{1 - i \sinh \left[2 \int_0^r B_0(z') dz' \right]} \quad (35)$$

Using Eq. (32), we can approximately solve the integrals and obtain the total transmission amplitude

$$T(\infty) \xrightarrow{OD_b \rightarrow \infty} T_0(\infty) + T_1(\infty) = i \left(1 - \frac{3\sqrt{2}\pi}{2} OD_b^{-3/2} \right), \quad (36)$$

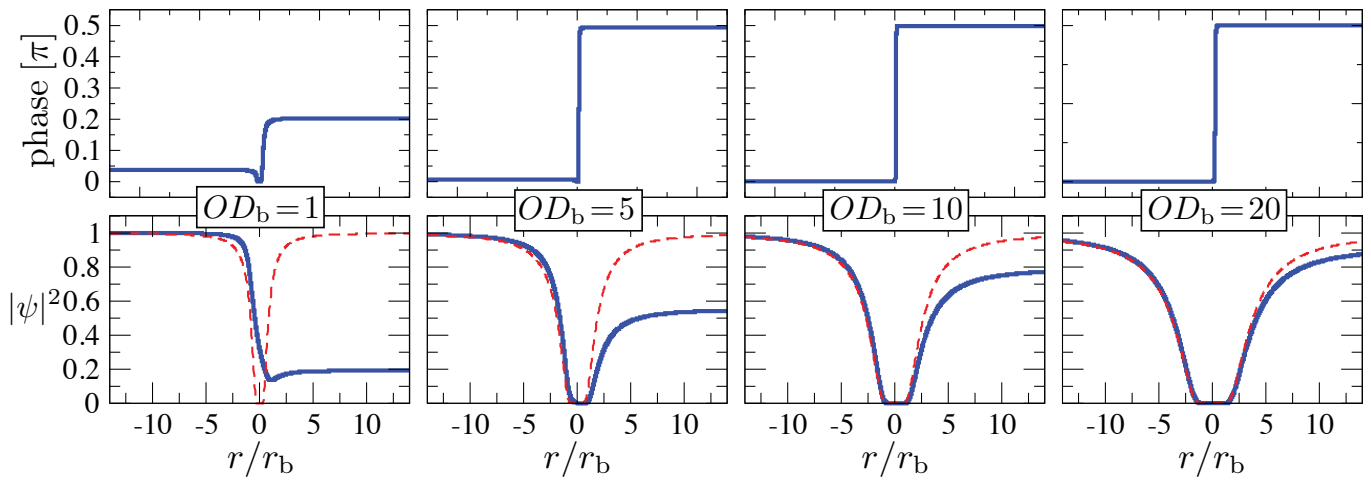


FIG. S3: Two-body phase (top) and probability density (bottom) as a function of the distance between the signal photon and the gate spin wave for different indicated values of optical depth per blockade radius, OD_b . The blue solid line shows numerical results while the red dashed line is obtained from the approximate solution Eq. (33).

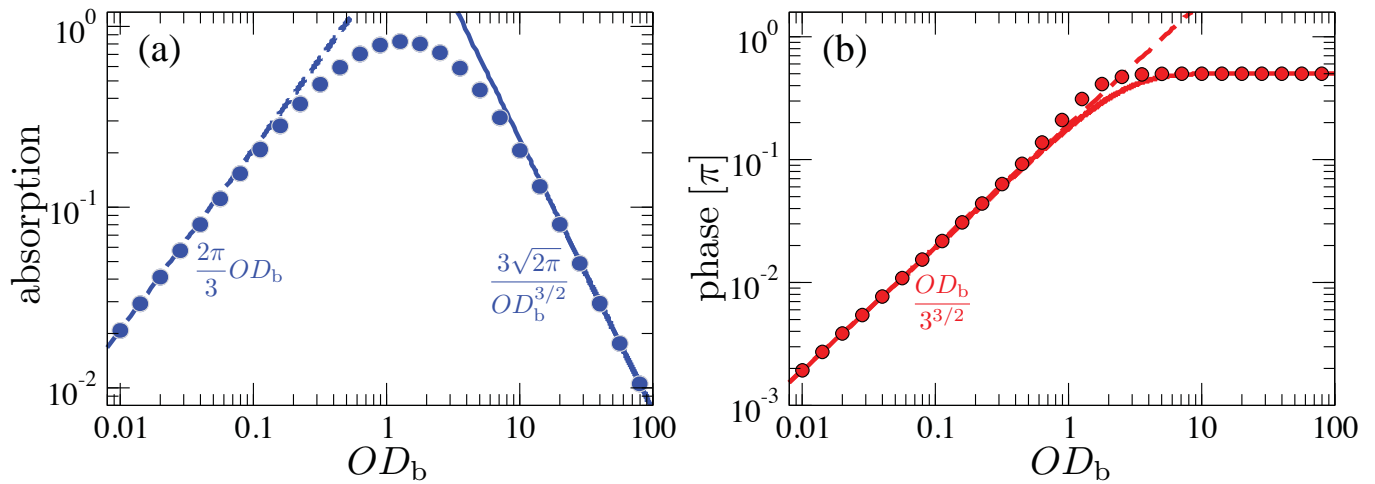


FIG. S4: (a) Signal photon absorption and (b) acquired phase as a function of OD_b . Symbols show numerical results while the solid and dashed lines show the asymptotic large- OD_b [Eqs. (36) and (33)] and small- OD_b [Eq. (37)] solutions, respectively.

which shows that the photon loss asymptotically decreases as $1 - |T|^2 = 3\sqrt{2\pi}OD_b^{-3/2}$ for large OD_b .

Similarly we can perform a perturbative expansion in the simpler limit of $OD_b \ll 1$, which gives $T_0 = 1$ to zeroth order in OD_b , and

$$T(\infty) \xrightarrow{OD_b \rightarrow 0} T_0(\infty) + T_1(\infty) = 1 - \frac{\pi}{3} \left(1 - \frac{i}{\sqrt{3}}\right) OD_b. \quad (37)$$

As shown in Fig. S4, the derived scaling laws quantitatively reproduce our numerical results in both relevant limits.

C. Propagation effects

With the outlined formalism, the leading-order inclusion of propagation effects becomes straightforward. To this end we now consider a finite medium of constant density and length $2L$ extending from $-L$ to L . Repeating the above

derivation, with A_0 replaced by $A_0 - iK - i\omega/v_g$, gives the following asymptotic ($r > r_s$) solution of Eq. (35)

$$\begin{aligned} T(r, K, \omega) &= i \left(1 - \frac{3\sqrt{2\pi}}{2} OD_b^{-3/2} \right) + 2(K + \omega/v_g)(r - \sqrt{\pi OD_b/2} r_b) \\ &\approx i \left(1 - \frac{3\sqrt{2\pi}}{2} OD_b^{-3/2} \right) e^{-2i(K + \omega/v_g)(r - \sqrt{\pi} r_s)}. \end{aligned} \quad (38)$$

Using the last expression in $\psi(r, K, \omega) = T(r, K, \omega)\psi(-r, K, \omega)$ and applying the free propagator, $\psi(r', K, \omega) = e^{-i(K + \omega/c)(r' - r)}\psi(r', K, \omega)$ for $r, r' \gg r_s$, then lets us Fourier transform back to time t and R and write the outgoing two-body state as

$$\psi(z = L, z', t) = i \left(1 - \frac{3\sqrt{2\pi}}{2} OD_b^{-3/2} \right) C(z' + \sqrt{\pi} r_s) E_{\text{in}} \left(t - \frac{L - \sqrt{\pi} r_s}{v_g} \right) \quad (39)$$

in terms of the initial spin wave profile $C(z)$ and the incident signal-field mode $E_{\text{in}}(t)$. We see that the dipole-dipole interaction does not cause any pulse distortion but gives rise to a homogenous spatial shift $\sqrt{\pi} r_s$. Note that the above derivation is only accurate to leading order in the bandwidth of both photons and, thus, requires that the spatial extent of the gate spin wave and the EIT-compressed signal photon pulse are both substantially larger than r_s . As a consequence the ideal scenario, Eq. (39), eventually deviates from the exact behavior as the optical depth per blockade radius is increased to too large values (see Fig.S5).

D. Derivation of Eq.(1) in the main text

Having established the vanishing of the two-body wave function for distances below $r_s = \sqrt{OD_b/2} r_b$, we can use an asymptotic $r/r_b \rightarrow \infty$ expansion of the coefficients Eq. (26) to simplify the propagation equations (25) in the limit of $OD_b \gg 1$. With the definition of r_b , this is equivalent to a Taylor expansion in $V_{ex}(r)/(\Omega^2/\gamma) \ll 1$ which yields

$$A(K, \omega) \approx -iK - i\frac{\omega}{v_g}, \quad B(r) \approx \frac{\bar{g}^2}{c\Omega^2} V_{ex}(r) \quad (40)$$

to linear order in $\omega/(\Omega^2/\gamma)$ and $V_{ex}/(\Omega^2/\gamma)$. With these expressions Eq. (25) simplifies to

$$\partial_r \psi(\pm r, K, \omega) = \mp iK \psi(\pm r, K, \omega) \mp i\frac{\omega}{v_g} \psi(\pm r, K, \omega) \pm i\frac{\bar{g}^2}{c\Omega^2} V_{ex}(r) \psi(\mp r, K, \omega) \quad (41)$$

Using $\bar{g}^2 \gg \Omega^2$ and Fourier transforming back to t and R we thus obtain

$$\partial_r \psi(\pm r, R, t) = \pm \partial_R \psi(\pm r, R, t) \pm v_g^{-1} \partial_t \psi(\pm r, R, t) \pm i v_g^{-1} V_{ex}(r) \psi(\mp r, R, t) \quad (42)$$

and in terms of z and z'

$$\partial_t \psi(z, z', t) = -\partial_z \psi(z, z', t) - i V_{ex}(z - z') \psi(z', z, t), \quad (43)$$

which coincides with Eq.(1) of the main text. Its stationary solution, presented in the main text, agrees with Eq.(33), as expected.

Following these arguments, the asymptotic treatment of the wave function for $r \gg r_b$ is equivalent to a perturbative expansion for small interactions $V_{ex} \ll \Omega^2/\gamma$. Under this condition the photon propagation can be described in terms of a dark-state polariton which follows Eq.(43). For $OD_b \gg 1$, the exchange-driven photon collision can thus be understood as a collision between dark-state polaritons. In contrast to previous Rydberg-EIT schemes where the van der Waals interaction inevitably causes coupling to bright state polaritons at distances $r \lesssim r_b$, such processes are inhibited by the long-range hopping at a distance $r_s \gg r_b$. This mechanism is key to the observed low photon losses.

V. MODELING THE COMPLETE EXPERIMENT

Now we turn to producing a complete model for the experiment, including finite pulse duration and bandwidth effects, dephasing, and the finite size of the atomic cloud. At the end, we present numerical simulations of this model to compare to the experimental results. To begin, we divide the experimental sequence into three stages:

- A.** the gate-photon storage into a nS -Rydberg spinwave and microwave transfer to a $n'P$ Rydberg state, creating a $n'P$ spinwave excitation at time $t = 0$,
- B.** its interaction with the incident signal photon extending from $t = 0$ to $t = T$,
- C.** followed by back-transfer of the gate excitation to an nS -Rydberg spin wave and subsequent retrieval ($t \geq T$),
- which we will describe separately below. The timing of the different stages and associated computational steps is illustrated in Fig. S6.

We extend the Heisenberg equations (19-22) to include dephasing and detuning terms, as well as inhomogeneous atomic density:

$$(\partial_t + c\partial_z)\hat{\mathcal{E}}(z, t) = -ig\sqrt{\rho(z)}\hat{\mathcal{P}}(z, t) \quad (44)$$

$$\partial_t\hat{\mathcal{P}}(z, t) = -ig\sqrt{\rho(z)}\hat{\mathcal{E}}(z, t) - i\Omega\hat{\mathcal{S}}(z, t) - \gamma\hat{\mathcal{P}}(z, t) \quad (45)$$

$$\begin{aligned} \partial_t\hat{\mathcal{S}}(z, t) = & -i\Omega\hat{\mathcal{P}}(z, t) - i[\Delta_s(z) - i\gamma_s]\hat{\mathcal{S}}(z, t) \\ & - i \int dz' V_{ex}(z - z')\hat{\mathcal{C}}^\dagger(z', t)\hat{\mathcal{C}}(z, t)\hat{\mathcal{S}}(z', t) \end{aligned} \quad (46)$$

$$\partial_t\hat{\mathcal{C}}(z, t) = -i\Delta_c(z)\hat{\mathcal{C}}(z, t) - i \int dz' V_{ex}(z - z')\hat{\mathcal{S}}(z', t)^\dagger\hat{\mathcal{S}}(z, t)\hat{\mathcal{C}}(z', t) \quad (47)$$

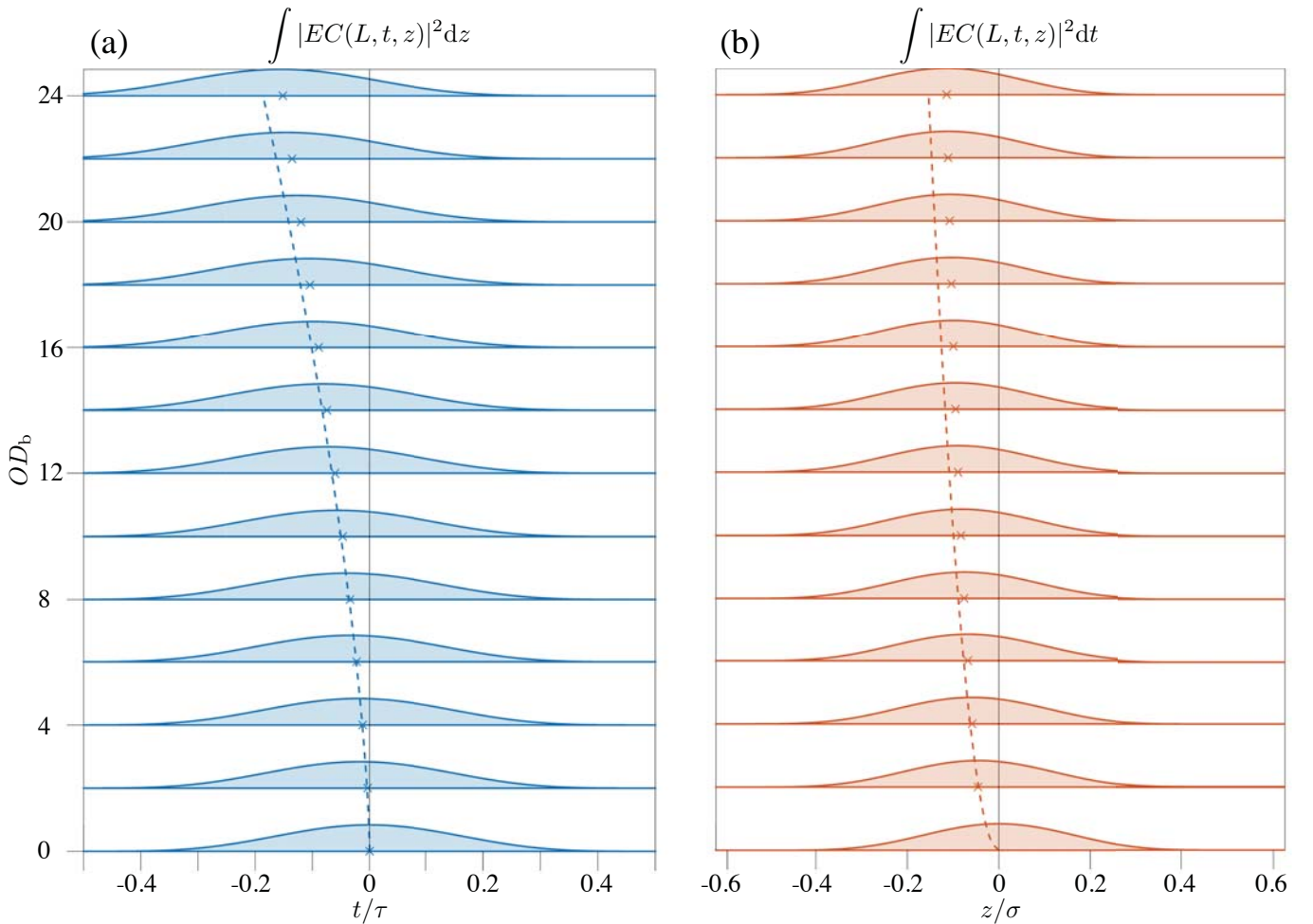


FIG. S5: (a) Transmitted signal photon intensity and (b) final probability density of the gate spin wave for different values of OD_b . The numerical simulations have been performed for a signal pulse duration of $\tau = 400(\Omega^2/\gamma)^{-1}$, a gate spin wave of length $\sigma = 40r_b$, $v_g/c = 0.01$ and $\Omega/\gamma = 1$. The crosses mark the numerical center of the photon pulse and spinwave density and the dashed lines show the analytical prediction Eq. (39).

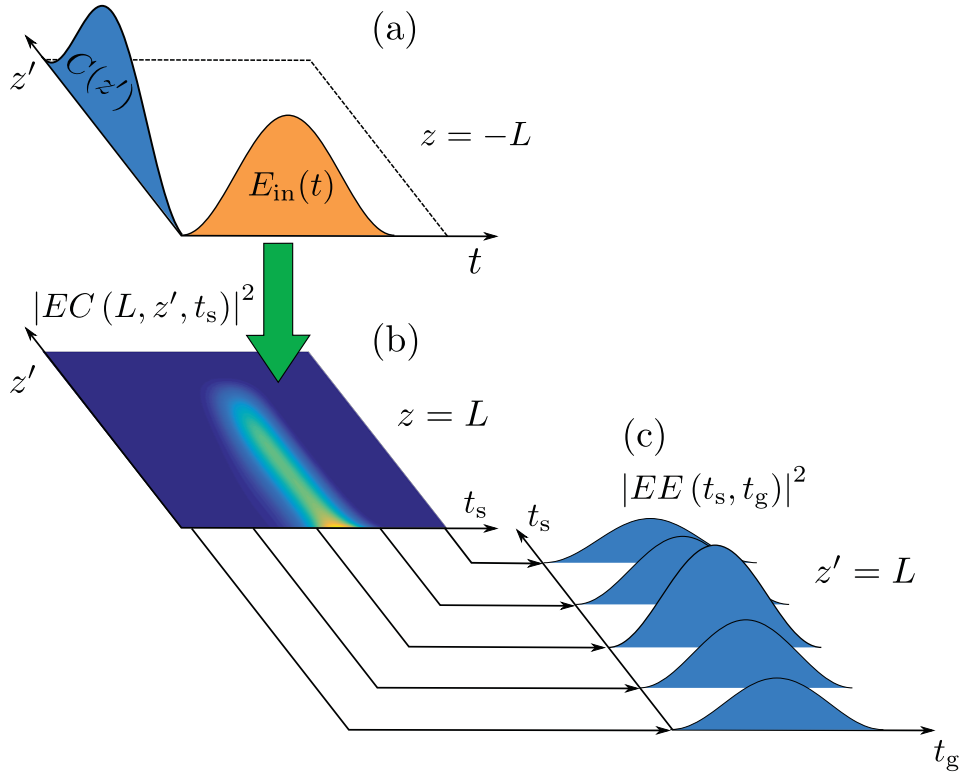


FIG. S6: Schematic illustration of photon collision sequence and involved computational steps. (a) Following the storage of a gate photon in a spin-wave mode $C(z')$, the signal photon enters the EIT medium at ($z = -L$) with a temporal pulse envelope $E_{\text{in}}(t)$. (b) During the interaction stage the correlated dynamics of the signal photon and the gate spin wave is described by the two-body amplitude $EC(z, z', t)$. Upon detection the transmitted signal photon at $z = L$ and a time t_s , the gate spinwave is left in a mode $EC(L, z', t_s)$. At each exit time t_s this amplitude is used as an initial condition for retrieval of the gate spinwave. (c) At each detection time t_s this amplitude provides the initial condition for determining the amplitude of the outgoing gate photon detected at time t_g , from which we obtain the two-photon amplitude $EE(t_s, t_g)$.

The atomic density $\rho(z) = \rho_0 f(z)$ has a Gaussian $f(z) = e^{-z^2/(2\sigma^2)}$ profile along the propagation axis, with a spatial width σ and peak density ρ_0 . g is the bare atom-light coupling. The position-dependent detunings $\Delta_s(z)$ and $\Delta_c(z)$ for the nS and $n'P$ states arise from interactions between ground state atoms and the excited Rydberg atoms, which vary according to the ground-state atomic density as discussed in section VII. γ_s accounts for the linewidth of the nS Rydberg state.

A. Gate photon storage

The signal photon is first stored in a Rydberg spin wave in the nS state and transferred to a $n'P$ excitation as described in the main text. Since our experiment uses a weak coherent pulse, it suffices to retain only the vacuum component, $\epsilon_g(t)|0\rangle$ and the single-excitation component

$$|\psi_g(t)\rangle = \int dz C(z, t) \hat{C}^\dagger(z) |0\rangle \quad (48)$$

of the produced spin wave state, where the amplitude $C(z, t = 0)$ denotes the mode profile of the spin wave right after storage. To simplify notation we further approximate $\epsilon_g(t) \sim 1$.

B. Interaction stage

Due to the dipolar excitation exchange, the propagation of the subsequent signal pulse requires a two-body treatment, even though the stored $n'P$ excitation is not coupled by the classical control field Ω . Again, retaining only

the vacuum and single-photon components of the incident signal pulse, the pure contribution to the total state of the system can be written as

$$|\Psi(t)\rangle = |0\rangle + |\psi_g(t)\rangle + |\psi_s(t)\rangle + |\psi_2(t)\rangle. \quad (49)$$

Impure parts resulting from the intermediate state decay do not need to be considered since the resulting spinwave decoherence precludes subsequent retrieval of the gate photon [4] and, thus, do not contribute to the observables discussed below.

The single spin wave state, $|\psi_g(t)\rangle$ is given by Eq. (48) with:

$$C(z, t) = C(z, t = 0) \exp[-i\Delta_c(z)t] \quad (50)$$

which follows from Eq. (47).

The wave function of the signal photon in the absence of a stored Rydberg excitation can be written as

$$|\psi_s(t)\rangle = \int dz E_s(z, t) \hat{\mathcal{E}}^\dagger(z) |0\rangle + \int dz P(z, t) \hat{\mathcal{P}}^\dagger(z) |0\rangle + \int dz S(z, t) \hat{\mathcal{S}}^\dagger(z) |0\rangle. \quad (51)$$

The evolution equations for the respective amplitudes $E_s(z, t) = \langle 0 | \hat{\mathcal{E}}(z) | \psi_s(t) \rangle$, $P(z, t) = \langle 0 | \hat{\mathcal{P}}(z) | \psi(t) \rangle$, and $S(z, t) = \langle 0 | \hat{\mathcal{S}}(z) | \psi(t) \rangle$ follows from Eqs. (44-46) and are given by

$$\begin{aligned} (\partial_t + c\partial_z)E_s(z, t) &= -ig\sqrt{\rho(z)}P(z, t) \\ \partial_t P(z, t) &= -ig\sqrt{\rho(z)}E_s(z, t) - i\Omega S(z, t) - \gamma P(z, t) \\ \partial_t S(z, t) &= -i\Omega P(z, t) - i[\Delta_s(z) - i\gamma_s]S(z, t). \end{aligned} \quad (52)$$

These equations are solved numerically within a spatial range $-L \leq z \leq L$. Assuming that the signal photon initially ($t = 0$) resides outside of this region at $z < -L$ and taking $L \gg \sigma$ such that $\rho(\pm L) \approx 0$, the initial and boundary conditions are $E_s(z, 0) = P(z, 0) = S(z, 0) = 0$ and $E_s(-L, t) = E_{\text{in}}(t)$, where $E_{\text{in}}(t)$ defines the temporal envelope of the incident signal pulse.

The two-body wavefunction is defined in Eq. (23). Its evolution is follows from substitution into Eqs. (44-47):

$$\begin{aligned} (\partial_t + c\partial_z)EC(z, z', t) &= -ig\sqrt{\rho(z)}PC(z, z', t) - i\Delta_c(z')EC(z, z', t) \\ \partial_t PC(z, z', t) &= -ig\sqrt{\rho(z)}EC(z, z', t) - i\Omega SC(z, z', t) - \gamma PC(z, z', t) \\ &\quad - i\Delta_c(z')PC(z, z', t) \\ \partial_t SC(z, z', t) &= -i\Omega PC(z, z', t) - i[\Delta_s(z) - i\gamma_s]SC(z, z', t) \\ &\quad - i\Delta_c(z')SC(z, z', t) - i\frac{C_3}{|z - z'|^3}SC(z, z', t). \end{aligned} \quad (53)$$

The initial conditions for $-L \leq z, z' \leq L$ are $EC(z, z', t = 0) = PC(z, z', t = 0) = SC(z, z', t = 0)$. Since the two-body amplitudes factorize for $z < -L$, we have the boundary condition $EC(-L, z', t) = E_{\text{in}}(t)C(z, t)$ where $C(z, t)$ is given by Eq. (50). The simultaneous numerical solution of Eqs.(50), (52) and (53), with the described initial and boundary conditions, thus yields completes knowledge about the two-body state Eq.(49).

A photodetector placed at $z = L$ then registers an outgoing signal photon at time t_s with a probability

$$\langle \hat{\mathcal{E}}^\dagger(L, t_s) \hat{\mathcal{E}}(L, t_s) \rangle = \langle \Psi(t_s) | \hat{\mathcal{E}}^\dagger(L) \hat{\mathcal{E}}(L) | \Psi(t_s) \rangle \equiv \langle \tilde{\Psi}(t_s; t_s) | \tilde{\Psi}(t_s; t_s) \rangle, \quad (54)$$

where

$$|\tilde{\Psi}(t_s; t_s)\rangle = E_s(L, t_s)|0\rangle + \int dz EC(L, z, t_s) \hat{\mathcal{C}}^\dagger(z)|0\rangle. \quad (55)$$

The amplitude of the spin-wave component after signal-photon detection still picks up a phase due to the random level shift $\Delta_c(z)$, such that the state of the system at the end of the interaction stage ($t = T$) is given by

$$|\tilde{\Psi}(T; t_s)\rangle = \epsilon_g(t_s)E_s(L, t_s)|0\rangle + \int dz EC(L, z, t_s) e^{-i\Delta_c(z)(T-t_s)} \hat{\mathcal{C}}^\dagger(z)|0\rangle. \quad (56)$$

C. Spinwave retrieval

Following the interaction stage, the stored $n'P$ spin wave is transferred back to an nS excitation and finally retrieved by turning the classical control field back on. The probability to detect the retrieved gate-photon at time t_g in the absence of a signal photon is given by $|E_g(L, t_g)|^2$, where the amplitude is determined by the single-photon propagation equations

$$\begin{aligned}(\partial_t + c\partial_z)E_g(z, t) &= -ig\sqrt{\rho(z)}P(z, t) \\ \partial_t P(z, t) &= -ig\sqrt{\rho(z)}E_g(z, t) - i\Omega S(z, t) - \gamma P(z, t) \\ \partial_t S(z, t) &= -i\Omega P(z, t) - i[\Delta_s(z) - i\gamma_s]S(z, t).\end{aligned}\quad (57)$$

subject to the initial $E_g(-L, t) = P(-L, t) = S(-L, t) = 0$ and initial conditions $E_g(z, T) = P(z, T) = 0$ and $S(z, T) = C(z, T)$, where $C(z, T)$ is given by Eq. (50).

Similarly, the amplitude of the retrieved photon after detection of a signal photon at time t_s is obtained from the evolution equations

$$\begin{aligned}(\partial_t + c\partial_z)E_2(z, t; t_s) &= -ig\sqrt{\rho(z)}P(z, t; t_s) \\ \partial_t P(z, t; t_s) &= -ig\sqrt{\rho(z)}E_2(z, t; t_s) - i\Omega S(z, t; t_s) - \gamma P(z, t; t_s) \\ \partial_t S(z, t; t_s) &= -i\Omega P(z, t; t_s) - i[\Delta_s(z) - i\gamma_s]S(z, t; t_s).\end{aligned}\quad (58)$$

with the boundary conditions $E_2(-L, t; t_s) = P(-L, t; t_s) = S(-L, t; t_s) = 0$ and initial conditions $E_2(z, T; t_s) = P(z, T; t_s) = 0$ and $S(z, T; t_s) = EC(L, z, t_s)e^{-i\Delta_c(z)(T-t_s)}$ [see Eq. (56)]. For each signal photon detection time t_s we thus have to propagate the one-body dynamics of the gate photon to finally obtain the two-time amplitude

$$EE(t_s, t_g) = E_2(L, t_g; t_s) \quad (59)$$

for detecting both photons at times $t_s < T$ and $t_g > T$.

VI. OBTAINING OBSERVABLES FROM NUMERICAL SIMULATIONS

In the following we describe how our observables presented in the main text are obtained from the two-time amplitude Eq. (59).

A. Conditioned signal photon transmission

It follows from the above discussion that the two-time correlation function

$$\langle \hat{\mathcal{E}}^\dagger(L, t_s) \hat{\mathcal{E}}^\dagger(L, t_g) \hat{\mathcal{E}}(L, t_g) \hat{\mathcal{E}}(L, t_s) \rangle = |EE(t_s, t_g)|^2 \quad (60)$$

is simply given by the joint probability Eq. (59). The signal photon transmission conditioned on detecting a gate photon is, thus, proportional to integral $\int dt_s dt_g |EE(t_s, t_g)|^2$. To calculate the relative transmission presented in the main text we have to compare this quantity to the equivalent result without interactions, for which $EE(t_s, t_g) = E_s(t_s)E_g(t_g)$ [obtained from Eq. (52) and Eq. (57)], giving the conditioned relative transmission

$$T_c = \frac{\int dt_s dt_g |EE(t_s, t_g)|^2}{\int dt_s dt_g |E_s(t_s)|^2 |E_g(t_g)|^2}, \quad (61)$$

shown in Fig. 3 of the main text. Similarly, we can calculate the outgoing pulse shape of the signal photon

$$I_s(t) = \int dt_g |EE(t, t_g)|^2, \quad (62)$$

and the gate photon

$$I_g(t) = \int dt_s |EE(t_s, t)|^2. \quad (63)$$

The comparison to our measured photon pulses in Fig. S7 demonstrates that the simulations even reproduce such more sensitive observables remarkably well.

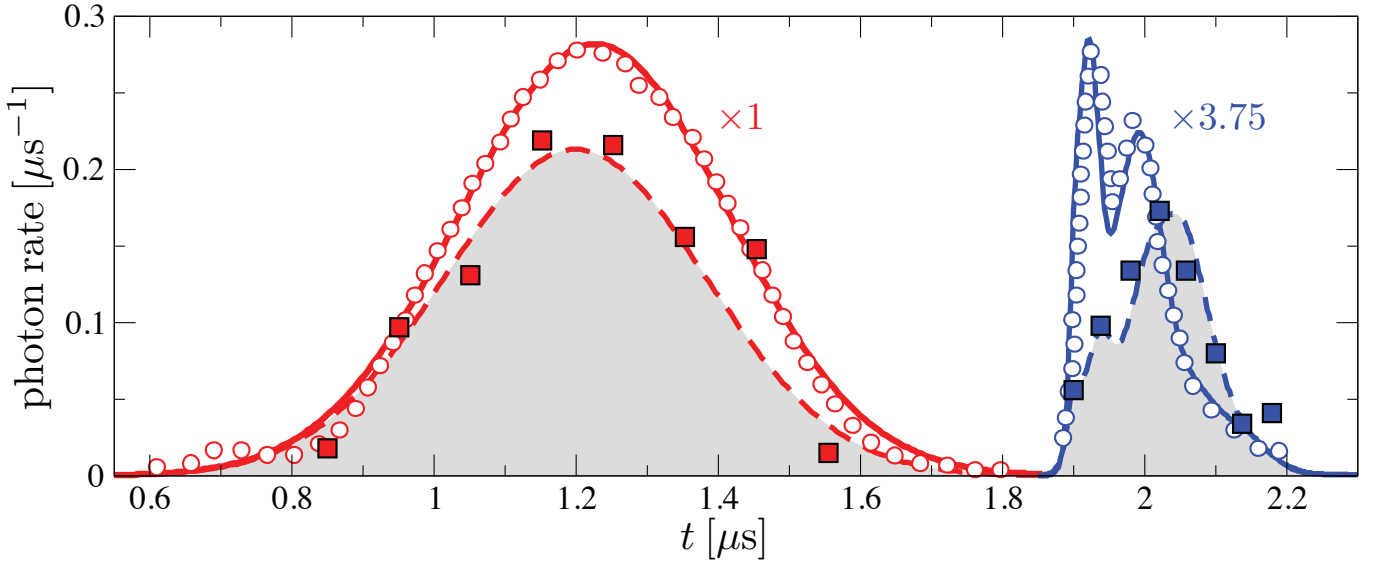


FIG. S7: Photon count rates of the signal photon (red) and retrieved gate photon (blue), measured in the presence (squares) and in the absence (circles) of dipolar excitation exchange. The experimental count rates are compared to the simulated pulse envelopes with (dashed lines, grey area) and without (solid lines) interactions. Each set of red and blue curves has been scaled by a single common factor in order to convert from the theoretical pulse envelopes to the observed count rates.

B. Acquired phase of the signal photon

In order to obtain the phase of the transmitted signal photon we superimpose the output by a reference field that does not interact with the medium, as described in the Methods. Taking the reference field to be a weak coherent pulse with a mode function $E_{\text{ref}}(z, t)$, its quantum state can again be approximated by

$$|\psi_{\text{ref}}(t)\rangle \approx |0\rangle + \int dz E_{\text{ref}}(z, t) \mathcal{E}^\dagger(z) |0\rangle. \quad (64)$$

Since all involved photon pulses are weak coherent fields, we can moreover discard any three-body contributions to the combined state $|\Psi_3(t)\rangle = |\Psi(t)\rangle |\psi_{\text{ref}}(t)\rangle$, with $|\Psi(t)\rangle$ given by Eq. (49). Upon detection of a signal photon at time t_s we thus get

$$\begin{aligned} \hat{\mathcal{E}}(L) |\Psi_3(t_s)\rangle &= [E_s(L, t_s) + E_{\text{ref}}(L, t_s)] |0\rangle + \int dz E_{\text{ref}}(z, t_s) E_s(L, t_s) \mathcal{E}^\dagger(z) |0\rangle \\ &+ \int dz E_{\text{ref}}(L, t_s) \left[C(z, t_s) \hat{\mathcal{C}}^\dagger(z) + P(z, t_s) \hat{\mathcal{P}}^\dagger(z) + S(z, t_s) \hat{\mathcal{S}}^\dagger(z) \right] |0\rangle \\ &+ \int dz E_{\text{ref}}(L, t_s) E_s(z, t_s) \hat{\mathcal{E}}^\dagger(z) |0\rangle + \int dz EC(L, z, t_s) \hat{\mathcal{C}}^\dagger(z) |0\rangle \end{aligned} \quad (65)$$

Taking this to be the initial state $|\bar{\Psi}_3(t = t_s; t_s)\rangle = \hat{\mathcal{E}}(L) |\Psi_3(t_s)\rangle$ for the description of the subsequent spin wave retrieval as described in section VC, we obtain after detection of a photon at time t_g

$$\begin{aligned} \hat{\mathcal{E}}(L) |\bar{\Psi}_3(t_g; t_s)\rangle &= E_{\text{ref}}(L, t_g) E_s(L, t_s) |0\rangle + E_{\text{ref}}(L, t_s) E_s(L, t_g) |0\rangle \\ &+ E_{\text{ref}}(L, t_s) E_g(L, t_g) |0\rangle + EE(t_s, t_g) |0\rangle \end{aligned} \quad (66)$$

Noting that $E_{\text{ref}}(L, t)$ and $E_s(L, t)$ both vanish for $t = t_g > T$, i.e. during the gate field detection window, we can drop the first line and obtain for the conditioned photon detection probability

$$\begin{aligned} \int_T^\infty dt_g \langle \hat{\mathcal{E}}^\dagger(L, t_s) \hat{\mathcal{E}}^\dagger(L, t_g) \hat{\mathcal{E}}(L, t_g) \hat{\mathcal{E}}(L, t_s) \rangle &= |E_{\text{ref}}(L, t_s)|^2 |E_g(L, t_g)|^2 + |EE(t_s, t_g)|^2 \\ &+ 2\text{Re} [E_{\text{ref}}^*(L, t_s) E_g^*(L, t_g) EE(t_s, t_g)]. \end{aligned} \quad (67)$$

The relative phase between the signal and reference field can be read off directly from the last line. Taking the reference field amplitude to be real this phase is given by

$$\varphi(t_s) = \arctan \left\{ \frac{\text{Im} \left[\int_T^\infty dt_g E_g^*(L, t_g) EE(t_s, t_g) \right]}{\text{Re} \left[\int_T^\infty dt_g E_g^*(L, t_g) EE(t_s, t_g) \right]} \right\}. \quad (68)$$

Even in the absence of interactions, for which $EE(t_s, t_g) = E_s(L, t_s)E_g(L, t_g)$, one will detect a density-dependent phase

$$\varphi_0(t_s) = \arctan \left\{ \frac{\text{Im} E_s(t_s)}{\text{Re} E_s(t_s)} \right\}. \quad (69)$$

which is predominantly due to the random level shifts $\Delta_s(z)$ in Eq. (52). Since this phase is taken as a reference in our experiments, the calculated phase

$$\phi_c = \int dt [\varphi(t) - \varphi_0(t)] I_s(t), \quad (70)$$

shown in Fig. 3 of the main text, is obtained by averaging the phase difference over the conditioned transmitted signal intensity given in Eq. (62).

VII. SPIN WAVE DEPHASING DUE TO RYDBERG-GROUND STATE ATOM INTERACTIONS

Here we describe how we account for interactions between Rydberg and ground state atoms through the random energy shifts $\Delta_c(z)$ and $\Delta_s(z)$. Such interactions arise when a ground state atom is found within the electronic orbit of the Rydberg atom, and perturbs the electronic wave function of the Rydberg state through a low-energy electron-atom collision [5, 6]. The collisional electron interaction, $\hat{U}_{e-a}(\mathbf{R})$, with an atom at a position \mathbf{R} away from the ionic core of the Rydberg atom then couples different Rydberg states $|\alpha\rangle$, $|\beta\rangle$ (with amplitudes $\psi_{\alpha,\beta}$) with a matrix element

$$\langle \beta | \hat{U}_{e-a}(\mathbf{R}) | \alpha \rangle = 2\pi A_s \psi_\beta^*(\mathbf{R}) \psi_\alpha(\mathbf{R}) + 6\pi A_p^3 [\nabla \psi_\beta^*(\mathbf{R})] \cdot [\nabla \psi_\alpha(\mathbf{R})]. \quad (71)$$

This can be well described via a zero-range pseudopotential [5] with energy-dependent s -wave and p -wave scattering lengths, A_s and A_p , respectively, whereby the electron energy can be semiclassically related to the scattering center \mathbf{R} [6, 7]. The shifted energy spectrum of the Rydberg atom can then be obtained by diagonalizing the underlying Hamiltonian $E_\alpha^{(0)} \delta_{\alpha,\beta} + \langle \beta | \hat{U}_{e-a}(\mathbf{R}) | \alpha \rangle$, where $E_\alpha^{(0)}$ is the unperturbed binding energy of the Rydberg atom in a given state $|\alpha\rangle$.

In the present situation, multiple ground state atoms may simultaneously shift a Rydberg state in the dense atomic cloud. The energy levels, $E_\alpha(\mathbf{R}_1, \dots, \mathbf{R}_N)$, collectively perturbed by N atoms at positions \mathbf{R}_i ($i = 1, \dots, N$) relative to the Rydberg atom core can still be straightforwardly obtained by diagonalizing the matrix $E_\alpha^{(0)} \delta_{\alpha,\beta} + \sum_{i=1}^N \langle \beta | \hat{U}_{e-a}(\mathbf{R}_i) | \alpha \rangle$.

To calculate the resulting level shift of a delocalized Rydberg state spin wave, we randomly sample atomic positions, \mathbf{r}_i , according to our density distribution $\rho(z)$ within a cylindrical volume along the light propagation axis, \mathbf{e}_z , assuming a constant density in the transverse direction. The spatially fluctuating energy shift $\Delta E_\alpha(z) = E_\alpha(\mathbf{r}_1 - \mathbf{e}_z z, \mathbf{r}_2 - \mathbf{e}_z z, \dots) - E_\alpha^{(0)}$ can then be calculated on the z -axis along which we solve the field propagation equations, as described in section V. As shown in Fig. S8, the mean level shift follows the atomic density [8], while the spatial fluctuations for a given random configuration are comparable to the actual average shift.

For the actual calculations we repeatedly simulate the two-photon dynamics as outlined in section V for a given random realization of $\Delta E_\alpha(z)$, and average the final observable over the Monte Carlo ensemble. Specifically, the conditioned transmission and the phase shown in Fig. 3 of the main text are determined as

$$T_c = \frac{\langle \int dt_s dt_g |EE(t_s, t_g)|^2 \rangle}{\langle \int dt_s dt_g |E_s(t_s)|^2 |E_g(t_g)|^2 \rangle}, \quad (72)$$

and

$$\phi_c = \left\langle \int dt [\varphi(t) - \varphi_0(t)] I_s(t) \right\rangle, \quad (73)$$

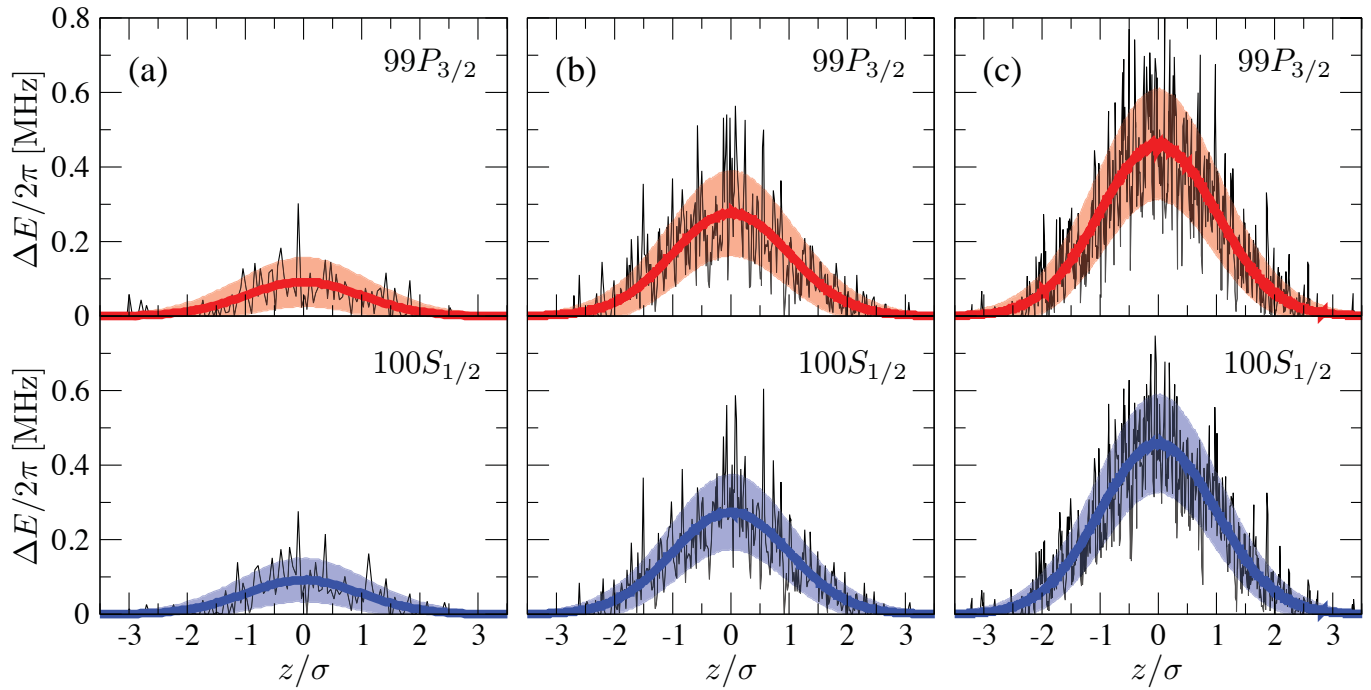


FIG. S8: Spatially fluctuating energy shifts due to interactions between Rydberg and ground-state atoms for the two relevant Rydberg states $|100S_{1/2}\rangle$ (blue) and $|99P_{3/2}\rangle$ (red) for the cloud geometry of our experiments and three different peak densities corresponding to $OD = 10$ (a), $OD = 30$ (b) and $OD = 50$ (c). The thick solid line shows the average level shift and the shaded area indicates the standard deviation of the ensemble. The individual Monte Carlo results shown by the thin black lines illustrate the strong spatial fluctuations in all cases.

respectively, where $\langle \dots \rangle$ denotes the Monte Carlo average over the ensemble of random atom configurations. Note that the shaded areas in Fig. 3 of the main text does not reflect the statistical error of the calculated average (which is small for the 10^4 configurations used in the calculation) but indicates the extent of the classical fluctuations of T_c and ϕ_c resulting from the randomly distributed atoms in the cold gas.

In our experiments we adjust the two-photon detuning to the transmission maximum of the EIT medium in the absence of the gate spin wave. Therefore, we first calculate the average transmission spectrum to determine the frequency shift, Δ_T , induced by Rydberg-ground state atom interactions for a given optical depth OD of the medium. The detunings Δ_s and Δ_c of Eqs.(46) and (47) are then obtained from

$$\Delta_\alpha(z) = \Delta E_\alpha(z) - \Delta_T \quad (74)$$

for the $|100S_{1/2}\rangle$ ($\alpha = s$) and the $|99P_{3/2}\rangle$ ($\alpha = c$) Rydberg states.

The Monte Carlo simulations also permit the role of Rydberg-ground state dephasing to be separated from other loss mechanisms. To this end we have simulated the photon propagation with and without the random level shifts Δ_s and Δ_c and calculated the reduction η of the two-photon transmission. The ratio $\eta/\eta^{(0)}$ of this reduction with (η) and without ($\eta^{(0)}$) dipolar excitation exchange (see Fig. S9), shows that the interaction significantly improves the performance of our protocol due to a motional averaging effect arising from the exchange-driven spin wave hopping. This effect improves the transmission by nearly a factor of two at the highest densities. Lastly, the simulations allow the effect of the mean shift (which follows the atomic cloud shape) to be separated from the fluctuating component of the shift which results from random atomic positions. At the highest densities used in the experiment, the mean shift contributes approximately half of the total dephasing of the retrieval, with the rest coming from “atomic shot noise”. While the mean shift does not change with the principal quantum number of the Rydberg level [8], the shot noise contribution decreases as n increases, since more ground state atoms participate and the fluctuations in their positions become less important.

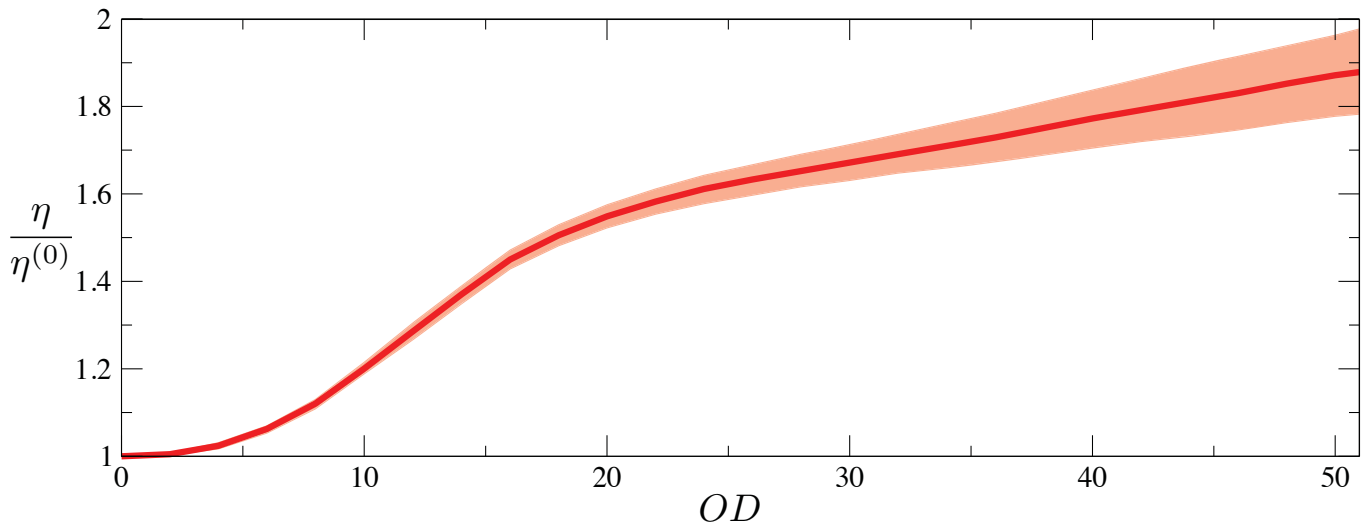


FIG. S9: The suppression, η , of the two-photon transmission by Rydberg-ground state atom interactions is significantly reduced by dipolar photon-spin wave hopping relative to the case of no interactions ($\eta^{(0)}$). The ratio $\eta/\eta^{(0)}$ is shown as function of OD , and for parameters of our experiments as used in Fig. 3 of the main text.

VIII. METHODS

A. Experimental procedure

The ^{87}Rb atoms used for this experiment are cooled in a 3D magneto-optical trap (MOT) and loaded into a 1064 nm crossed optical dipole trap made with two horizontal beams crossed at a 32° angle [9, 10]. Each beam has a power of 8 W and a $50\ \mu\text{m}$ waist, resulting in a cigar-shaped density profile with a 4:1 trap aspect ratio. After loading into the dipole trap, the gas is cooled to $20\ \mu\text{K}$ using degenerate Raman sideband cooling in a near-detuned lattice. The peak atomic density at the highest optical depth is approximately $\rho = 1.9 \times 10^{12}\ \text{cm}^{-3}$, which corresponds to a resonant absorption length of $1.8\ \mu\text{m}$ for the probe field. Cooling and loading last for 300 ms, and then 1000 measurements are performed with a repetition period of $38\ \mu\text{s}$ before preparing a new sample. The dipole trap is switched off during each measurement (for $7\ \mu\text{s}$) to avoid AC Stark shifts of the Rydberg levels. The gas is probed along the long axis of the cloud, as shown in Fig. 1.

The probe and control lasers are stabilized to a common cavity, and have a short-term linewidth of approximately $2\pi \times 100\ \text{kHz}$. The 3.72 GHz microwave field driving $100S_{1/2}$ to $99P_{3/2}$ is delivered by an antenna outside the vacuum chamber. For measurements involving other Rydberg states (Fig 3 insets), the microwave field drives a two-photon transition from $100S_{1/2}$ to $99S_{1/2}$ (at 3.67 GHz microwave frequency) or to $97S_{1/2}$ (at 11.4 GHz).

B. Phase-shift measurements

Phase-shift measurements are performed by interfering the transmitted probe field \mathcal{E} with a weak local oscillator (LO) beam, which is detuned by $-158\ \text{MHz}$ from the probe. The LO is delivered to the experiment through the same fiber as the probe, and has a similar intensity. This detuning and power ensure that the LO does not interact with the Rydberg levels, so any phase shift in the probe-LO beatnote arises from phase shifts in the probe field. The LO has a square pulse shape and is switched on at the same time as the signal pulse. The probe-LO beat signal is delivered to single-photon counting modules, and the beat amplitude and phase are extracted from the timing of photon detection events. A slight non-uniformity of the phase across the pulse (visible in the light points in Fig. 2D) appears to result from rate-dependent timing delays in the detectors. Zero phase in Fig. 2D is defined by a control experiment without interactions, achieved by setting $n_g^{in} = 0$. This phase is slightly different from the phase measured without any atoms present, and results from the effects of atomic dispersion on the far-detuned LO, as well as small phase shifts on the probe arising from a minority of atoms not prepared in $|F = 2, m_F = 2\rangle$. Lastly, because of the negative detuning of the LO, the positive phase shift of the beatnote that is shown in Fig. 2D/3B actually corresponds to a phase lag of the probe, in agreement with the negative phase shift predicted by the solution to Eq. (1) for $C_3 > 0$.

	$\tilde{\eta}_s$	$\tilde{\eta}_g$	$\tilde{\eta}_2$	η_I	η_2
current	0.56	0.06	0.034	0.8	0.027
improved	0.99	0.93	0.92	0.95	0.88

TABLE II: Summary of efficiency measurements. The single-photon transmission probabilities for the signal and gate fields, in the absence of interactions, are $\tilde{\eta}_s$ and $\tilde{\eta}_g$, respectively. The probability that two incident photons would both be transmitted in absence of interactions is $\tilde{\eta}_2 = \tilde{\eta}_s \tilde{\eta}_g$. Interactions result in an additional loss captured by η_I , such that the probability for two photons to be transmitted with a phase shift is $\eta_2 = \tilde{\eta}_s \tilde{\eta}_g \eta_I$. η_I was measured using the signal (gate) field to be 0.77 (0.82); here, we take the average value 0.80.

C. Photon loss

The losses in the experiment are largely technical in origin and can be reduced through several straightforward improvements. The losses are summarized in Table II, and the possible improvements are discussed below.

The linear (non-interacting) signal transmission $\tilde{\eta}_s = 0.56$ is limited primarily by laser linewidth and imperfect optical pumping of atoms to the $|2, 2\rangle$ state (atoms in other states will not experience EIT resonance at the same laser frequency). It should be possible to improve $\tilde{\eta}_s$ to nearly 1 by reducing the laser linewidth further and improving the optical pumping or applying a larger magnetic field to shift the absorption profiles of other ground states away from the probe laser frequency. Other dephasing effects, such as Doppler broadening and collisions between ground state atoms and Rydberg atoms (section VII) are slowly varying and produce a transmission decay that is Gaussian as a function of the time the photon spends in the cloud. For the signal photon, which is not stored, we estimate the impact of these effects on $\tilde{\eta}_s$ be less than 0.01 during the 180 ns transit time of the signal photon.

The linear (non-interacting) storage and retrieval efficiency is currently $\tilde{\eta}_g = 0.06$. Separate measurements show that the storage and retrieval efficiency with only 100 ns storage time is 0.4, which then decreases to 0.06 at the 1.5 μ s storage time needed to complete the interaction sequence. The storage and retrieval efficiency at short times is limited by the same effects as the signal transmission, as well as the finite optical depth: in Ref. [11] it is shown that the achievable storage and retrieval efficiency scales as $1 - 5.8/OD$ using optimized pulses and backwards retrieval. Therefore, this number could be improved to 0.84 with our current OD , and to 0.95 with OD doubled to 100.

The impact of the long storage time is more significant. The decrease in retrieval efficiency comes from dephasing of the stored spin wave, with contributions from Doppler broadening and collisions between ground state atoms and Rydberg atoms, as discussed in section VII. Doppler broadening can be significantly reduced by going to lower temperatures. The collisional dephasing contains two contributions: random atomic positions (atomic shot noise) within the Rydberg orbit, as well as non-uniform density envelope across the cloud. The latter can be improved using a flat-bottom optical potential (as discussed in [13]), while the atomic shot noise can be improved by moving to higher principal quantum number, which has the effect of increasing the number of ground state atoms involved but decreasing the contribution from each individual atom [8], reducing the shot noise as n^{-3} , where n is the principal quantum number. To make the (Gaussian) Doppler and collisional dephasing decays less than 2% each during the storage time of 1.5 μ s, we need to improve the temperature by a factor of 5, and the impact of the collisional dephasing by a factor of 10. In the latter case, a factor of two can be obtained from the flat-bottom potential, with the remaining factor of 5 coming from an increase in the principal quantum number to $n = 170$. Even with these changes, we will remain far from the regime where inelastic collisions with ground state atoms will play a role on the relevant timescales [12]. Together, these improvements can yield a storage and retrieval efficiency of about 0.93.

The additional losses resulting from the interaction process are shown in Eq. 36 to scale as $\eta_I = 1 - 3\sqrt{2\pi}OD_b^{-3/2}$, depending only on OD_b . To reach $\eta_I = 0.95$, we will require $OD_b = 30$. OD_b increases with $n^{4/3}$, so increasing the quantum number to 170 together with increasing the atomic density by a factor of 2.5 (through additional cooling or larger total atom number) will achieve the desired result. Reducing the control Rabi frequency Ω_c during the signal pulse will allow OD_b to be further increased, at the expense of increasing the required storage time—there is an optimum value.

Taken together, it seems realistic to achieve combined linear transmission for the signal and gate photon of 0.99 and 0.93, and nonlinear losses of 0.95. This would result in a total transmission probability for two interacting photons of 0.88. Given that the dominant error in the interaction process is photon loss and not error in the phase shift, and that photon loss can be heralded by the absence of transmitted photons, we expect that higher-fidelity operations can be probabilistically achieved.

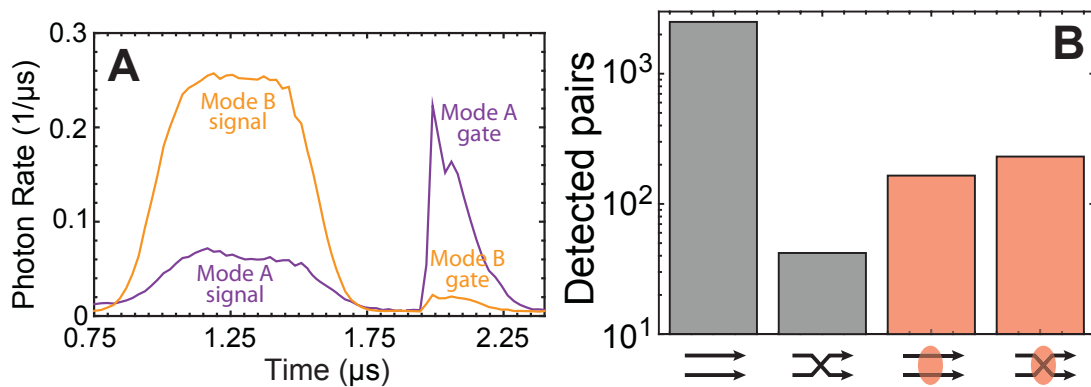


FIG. S10: A) Pulse shapes measured by the detectors shown in Fig. 4A of the main text. The full data record is averaged to produce these curves. B) Photon pair detection events. The parallel (crossed) arrows denote the number of signal and gate pairs detected in their incident (swapped) modes. The left two bars show the result of the alternate pulse sequence without interactions, while the right two bars show the result of the pulse sequence in panel A, where interactions are expected to be present. From left to right, the y-axis values are 2499, 42, 165, and 231.

D. Two-mode measurements

For the measurements in Fig. 4 with two optical modes, two independently-aligned beams (modes A, B) are nearly overlapped on a beamsplitter before entering the chamber. Their separation ($5.4 \mu\text{m}$) is measured using a CCD camera that images the focal plane in the center of the atomic cloud. The output light is directed to two single-mode fibers by a beamsplitter. One of the fibers is aligned to each mode, allowing them to be separately detected by independent photodetectors. There is a small amount of crosstalk resulting from imperfect fiber alignment and finite separation between the modes (about 10% of the light detected in the mode A photon counter is actually from mode B, and vice-versa).

E. Pair detection events in separated optical mode measurements

Here, we describe additional measurements used to estimate the probability of photons hopping between spatially separated modes as described in Fig. 4 of the main text. This measurement involves alternating between the pulse sequence shown in Fig S10A and another sequence where the signal pulse is sent after the gate pulse is retrieved. In the latter sequence, the signal and gate fields experience the same loss, but do not interact with each other as they are never present in the cloud at the same time. The difference between these measurements allows the influence of interactions to be isolated.

Fig S10A shows the measured pulse shapes at each detector (Fig. 4A). As in the main text, the gate (signal) pulse is incident in mode A (B). The majority of the light in the “wrong” detector (e.g., signal light in detector A) results from a slight mixing of the modes at the detectors (approximately 10%), since the modes are not perfectly orthogonal. To see the role of interactions above this background, we look at photon pair events as shown in Fig. S10B. Without interactions, approximately 1.7(3)% of all transmitted pairs are in “swapped” modes. With interactions, 58(2)% of pairs exit in swapped modes, although the overall transmission is much lower. In analogy with T_c defined in Fig. 3 of the main text, we isolate the role of interactions over single-particle loss by computing the ratio of the number of pairs exiting in swapped modes (with interactions) to the total number of transmitted pairs in the absence of interactions. This yields 8.3(5)%, which we take as an estimate of the probability for a photon pair to switch modes as a result of the interaction.

This value is significantly lower than $T_c = 0.77$ reported in Fig. 3 for photons in the same mode. We attribute this to increased separation between the photons, as well as losses resulting from multiple signal and gate photons being present during the same pulse, since this measurement was performed with $\langle n_g^{in} \rangle \approx \langle n_s^{in} \rangle \approx 1$.

[1] M. Saffman, T.G. Walker and K. Mølmer, Rev. Mod. Phys. **82**, 2313 (2010).

- [2] P. Bienias, S. Choi, O. Firstenberg, M.F. Maghrebi, M. Gullans, M.D. Lukin, A.V. Gorshkov and H.P. Büchler, *Phys. Rev. A* **90**, 053804 (2014).
- [3] M. Fleischhauer and M.D. Lukin, *Phys. Rev. Lett.* **84**, 5094 (2000).
- [4] C.R. Murray, A.V. Gorshkov and T. Pohl, arXiv:1607.01984
- [5] E. Fermi, *Nuovo Cimento* **11**, 157 (1934).
- [6] C.H. Greene, A.S. Dickinson and H.R. Sadeghpour, *Phys. Rev. Lett.* **85**, 2458 (2000).
- [7] E.L. Hamilton, C.H. Greene and H.R. Sadeghpour, *J Phys B* **35**, L199 (2002).
- [8] A. Gaj, A.T. Krupp, J. B. Balewski, R. Löw, S. Hofferberth and T. Pfau, *Nature Comm.* **5**, 4546 (2014).
- [9] T. Peyronel, O. Firstenberg, Q.-Y. Liang, S. Hofferberth, A.V. Gorshkov, T. Pohl, M.D. Lukin and V. Vuletic, *Nature* **488** 57 (2012).
- [10] O. Firstenberg, T. Peyronel, Q.-Y. Liang, A.V. Gorshkov, M.D. Lukin and V. Vuletic, *Nature* **502**, 71 (2012).
- [11] A.V. Gorshkov, A. Andre, M.D. Lukin, and A.S. Sorensen, *Phys. Rev. A* **76**, 033805 (2007).
- [12] M. Schlagmuller, T.C. Liebisch, F. Engel, K.S. Kleinbach, F. Bottcher, U. Hermann, K.M. Westphal, A. Gaj, R. Low, S. Hofferberth, and T. Pfau, *Phys. Rev. X* **6**, 031020 (2016).
- [13] D. Tiarks, S. Schmidt, G. Rempe, and S. Dürr, *Science Advances*, **2**, e1600036 (2016).